Nano Research
2020, 13(3): 709–718
ISSN 1998-0124 CN 11-5974/O4
https://doi.org/10.1007/s12274-020-2680-5

Research Article

Effects of crystal structure on the activity of MnO_2 nanorods oxidase mimics

Yanxia Meng[1,4], Kunfeng Zhao[2,3,4] (✉), Zhaokun Zhang[1,4], Peng Gao[5] (✉), Jing Yuan[3], Ting Cai[3], Qin Tong[3], Gang Huang[4], and Dannong He[2,4] (✉)

[1] *School of Medical Instrument and Food Engineering, University of Shanghai for Science and Technology, 516 Jungong Road, Shanghai 200093, China*
[2] *School of Materials Science and Engineering, Shanghai Jiao Tong University, 800 Dongchuan Road, Shanghai 200240, China*
[3] *National Engineering Research Center for Nanotechnology, 28 East Jiangchuan Road, Shanghai 200241, China*
[4] *Shanghai University of Medicine and Health Sciences, 279 Zhouzhu Road, Shanghai 201318, China*
[5] *Ningbo Fundenergy Co., Ltd., 699 Haicheng Road, Ningbo 315200, China*

Received: 21 November 2019 / **Revised:** 18 January 2020 / **Accepted:** 22 January 2020

ABSTRACT

The crystal structures would directly affect the physical and chemical properties of the surface of the material, and would thus influence the catalytic activity of the material. α-MnO_2, β-MnO_2 and γ-MnO_2 nanorods with the same morphology yet different crystal structures were prepared and tested as oxidase mimics using 3,3',5,5'-tetramethylbenzidine (TMB) as the substrate. β-MnO_2 that exhibited the highest activity had a catalytic constant of 83.75 μmol·m^{-2}·s^{-1}, 2.7 and 19.0 times of those of α-MnO_2 and γ-MnO_2 (30.91 and 4.41 μmol·m^{-2}·s^{-1}), respectively. The characterization results showed that there were more surface hydroxyls as well as more Mn^{4+} on the surface of the β-MnO_2 nanorods. The surface hydroxyls were conducive to the oxidation reaction, while Mn^{4+} was conducive to the regeneration of surface hydroxyls. The synergistic effect of the two factors significantly improved the activity of β-MnO_2 oxidase mimic. Using β-MnO_2, a β-MnO_2-TMB-GSH system was established to detect the content of glutathione (GSH) rapidly and sensitively by colorimetry. This method had a wide detection range (0.11–45 μM) and a low detection limit (0.1 μM), and had been successfully applied to GSH quantification in human serum samples.

KEYWORDS

crystal phase structure, MnO_2, oxidase mimics, surface hydroxyls, 3,3',5,5'-tetramethylbenzidine (TMB), glutathione

1 Introduction

Enzyme mimics (also known as "nano-enzymes") are widely used in biomolecular detection, such as glutathione, glucose, dopamine, aflatoxin, uric acid, etc [1–6]. Glutathione (GSH), found in almost every organism cell, is considered helpful to maintain a normal immune system and to play an important role in defending against toxins and scavenging free radicals [7, 8]. Many diseases are related to abnormal GSH level. For example, the lack of GSH can lead to white blood cell loss, cancer, AIDS, and neurodegenerative diseases [9–12]. Therefore, rapid, convenient and sensitive detection of GSH is of great significance in clinical diagnosis [10–13]. Due to the advantages of simple operation, low cost, free of complicated instruments and feasible for real-time field detection, enzyme-catalyzed biological colorimetry method has attracted wide attention in the fields of both biological science and analytical chemistry [14–18].

Compared with natural enzymes, enzyme mimics have superior characteristics, e.g. simple preparation, property stability, strong environmental tolerance, low manufacturing and storage costs, and thus are widely used in biomolecular detections [19, 20]. In recent years, MnO_2 has been attracting much attention because of its high activity and fine biological safety. In 2012, Liu et al. found that MnO_2 nanoparticles, as bio-enzymes substitute, could catalyze the oxidation of colorless 3,3',5,5'-tetramethylbenzidine (TMB, a typical enzyme substrate) to blue oxidized TMB (oxTMB) without H_2O_2, showing the activity of oxidase and significance in biological colorimetry [21]. The oxTMB has a typical absorption peak at the wavelength of 652 nm. As GSH can reduce MnO_2 to Mn^{2+} without oxidase activity and reduce oxTMB to TMB, the absorption peak intensity at the wavelength of 652 nm would become weaker. Also, the decrease of absorbance is linearly correlated with the GSH concentration of the solution added. Based on these, MnO_2-TMB-GSH systems has been established to detect the concentration of GSH and successfully applied to the detection of GSH in human serum samples [22, 23].

The crystal structure, morphology, particle size, specific surface area, valence state and surface element composition of enzyme mimics significantly affect their activities [24, 25]. Wan et al. compared and tested the oxidase activities of MnO_2 samples with different morphologies (nanosheets, nanospheres, nanowires and nanosticks) using TMB as substrate. They found that although MnO_2 nanowires and nanospheres had different morphologies, these two oxidase mimics had the highest

Address correspondence to Kunfeng Zhao, zhaokunfeng-gl@163.com; Dannong He, hdn_nercn@163.com; Peng Gao, gaop@fundenergy.com.cn

activity. Interestingly, while nanowires and nanosticks were of similar morphologies, the two showed significant performance differences [26]. Zhang et al. synthesized MnO_2 nanowires, MnOOH/MnO_2 nanorods and octahedral MnO_2 nanoparticles by hydrothermal method, and found that MnO_2 nanowires had high catalytic activity of oxidase mimics [23]. However, these studies failed to show the effects of crystal structure and surface chemistry on the activities of the enzyme mimics. So far, there have been only few, if any, reports on structure–activity relationship of MnO_2 oxidase mimics. The systematic and in-depth studies of the mechanism of various influencing factors are called for to better design and improve the performances of enzyme mimics. This is not only of scientific significance, but also of great importance in practical applications. Moreover, the research on MnO_2 oxidase mimics can also provide benefits for the design and development of other enzyme mimics.

In this study, α-MnO_2, β-MnO_2 and γ-MnO_2 nanorods with the same morphology yet different crystal structures were prepared and tested. β-MnO_2 that exhibited the highest activity had a catalytic constant of 83.75 $\mu mol \cdot m^{-2} \cdot s^{-1}$, 2.7 and 19.0 times of that of α-MnO_2 and γ-MnO_2 (30.91 and 4.41 $\mu mol \cdot m^{-2} \cdot s^{-1}$), respectively. The characterization results showed that the synergistic effect of surface hydroxyl groups and Mn^{4+} significantly improved the activity of β-MnO_2 oxidase mimic. Subsequently, GSH was detected by colorimetry using β-MnO_2, the oxidase mimic with the best activity. This detecting system had a wide detection range and a low detection limit. This paper provides a potential option to prepare high-efficiency enzyme mimics by modulating the crystal structures and surface physical-chemical properties.

2 Experimental

2.1 Preparation of MnO_2 in different crystal phases

MnO_2 nanorods in different crystal phases were prepared as the reported procedure [27, 28]. The specific steps were as follows. For α-MnO_2: 0.20 g of $MnSO_4 \cdot H_2O$ and 0.50 g of $KMnO_4$ were dissolved in 80 mL of Milli-Q water, and then 2 mL of concentrated HNO_3 was added into the above solution. After stirring for 0.5 h, the mixed solution was transferred into Teflon reactor and hydrothermally reacted at 140 °C for 12 h. For β-MnO_2: 75 mL of solution contained of 1.08 g of $MnSO_4 \cdot H_2O$ and 1.46 g of $(NH_4)_2S_2O_8$ was stirred for 0.5 h, transferred into Teflon reactor and hydrothermally reacted at 140 °C for 12 h. For γ-MnO_2: The γ-MnO_2 was synthesized from the hydrothermal reaction of 3.38 g of $MnSO_4 \cdot H_2O$ and 4.58 g of $(NH_4)_2S_2O_8$ dissolved in 80 mL of Milli-Q water at 90 °C for 24 h. The three precipitates obtained above were filtered, washed with Milli-Q water and ethanol until neutral, and dried in an oven at 80 °C overnight.

2.2 Characterization of MnO_2 in different crystal phases

The specific surface areas (S_{BET}) of MnO_2 oxidase mimics were detected by a Micromeritics ASAP 2020M physisorption instrument, USA. The X-ray diffraction (XRD) patterns were obtained by an X-ray diffractometer of the Japanese Science D/max-2600PC equipped with a Cu Kα line radiation source (λ = 1.5432 Å), operating at 45 kV and 40 mA. The diffractograms were recorded in a 2θ range from 10° to 80° at a scanning speed of 10 °·min^{-1}. Scanning electron microscopy (SEM) and transmission electron microscopy (TEM) images were acquired on a Hitachi S-4800 field emission scanning electron microscope and a JEM-2100F field emission transmission electron microscope from Japan JEOL, respectively. The hydrodynamic size and zeta potential of α, β, γ-MnO_2 were obtained by a dynamic light scattering (DLS) technique on Laser Particle Sizer (nano scale), UK. The X-ray photoelectron spectra (XPS) were obtained by an AXIS Ultra DLD X-ray photoelectron spectrometer from Shimadzu Kratos, Japan. A Mg-Kα rays were used as excitation source ($h\nu$ = 1,253.6 eV), and the chamber pressure was about 5×10^{-8} Pa. The carbon (C1s = 284.6 eV) was used as an internal standard to correct the charge effect of the sample. The H_2 temperature-programmed reduction (H_2-TPR) experiment was performed on an AutoChem II 2920 apparatus from Micromeritics, USA. The MnO_2 oxidase mimic (20 mg) was heated from 100 to 700 °C for reduction in 10% H_2/Ar mixture with a flow rate of 15 $mL \cdot min^{-1}$. The heating rate was 10 °C·min^{-1} and the outlet gas was detected online using a thermal conductivity detector (TCD). Electron spin resonance (ESR) signals of reactive oxygen species (ROS) in the process of TMB oxidation catalyzed by MnO_2 were investigated by Bruker model A300 spectrometer. 5,5-Dimethyl-1-pyrroline N-oxide (DMPO) and 2,2,6,6-tetramethylpiperidine (TEMP) were added into the MnO_2 catalyzed reaction systems to trap hydroxyl radicals (·OH) and superoxide radicals ($\cdot O_2^-$), and singlet oxygen ($^1O_2$). The signals of the spin adducts (DMPO/·OH, DMPO/$\cdot O_2^-$ and TEMP/$^1O_2$) were examined at the beginning of the reaction. All operations were carried out at room temperature.

2.3 Oxidase activities test of MnO_2 in different crystal phases

The activity test of MnO_2 oxidase mimic was performed in a batch reaction mode at 25 °C. Prior to test, 1 mL of NaAc-HAc buffer (pH 4.0) and 1 mL of 1.25 mM TMB were mixed evenly. Then the mixture was added into the colorimetric dish and placed in the detection box of UV–visible–near-infrared (UV–Vis–NIR) spectrophotometer. After adding 0.1 mL of 0.125 $g \cdot L^{-1}$ MnO_2 suspension, the absorbances at 652 nm of the reaction system as a function of time were detected immediately until there was almost no change occurred. Absorbance detection was performed on a Lambda 950 UV–Vis–NIR spectrophotometer from PerkinElmer, USA. The initial reaction rate was defined as the average reaction rate within 5 s which was calculated based on the Lambert-Beer law in which the extinction coefficient of oxTMB was 3.9×10^4 $M^{-1} \cdot cm^{-1}$ and the optical path was 1 cm. Special note was made in the corresponding position in this paper for any change.

To explore the effect of the produced ROS on TMB catalytic oxidation, p-dimethylsulfoxide (DMSO), superoxide dismutase (SOD) and 9,10-diphenylanthracene (DPA) were added into the reaction systems as scavengers for $\cdot O_2^-$, ·OH, and $^1O_2$, respectively. Besides, the sequential oxidation of TMB in N_2 and O_2 was performed further to verify the activity of surface hydroxyls of MnO_2 oxidase mimics.

2.4 Detection of GSH using β-MnO_2

Firstly, 1 mL of NaAc-HAc buffer (pH 4.0), 1 mL of 1.25 mM TMB solution and 0.1 mL of 0.125 $g \cdot L^{-1}$ β-MnO_2 suspension were mixed and reacted completely for 20 min at 25 °C. And then, 0.1 mL of GSH solution with different concentrations was added into the above β-MnO_2-TMB system for another 20 min. The absorbances at 652 nm of the system with and without GSH were both detected by UV–Vis–NIR spectrophotometer. The detection of glutathione can be realized from the relationship between the changes in absorbance and the concentrations of GSH.

2.5 Analysis of GSH in human samples by β-MnO_2-TMB system

The selectivity of β-MnO_2 oxidase mimics for GSH was studied by adding the bio-ions, glucose, ascorbic acid (AA), L(+)-cysteine (Cys) and other amino acids in human serum as interferents into the reaction system. After reaction at room temperature for 10 min, the absorbances at 652 nm of the systems were measured.

Human serum samples were obtained from a 30-year-old male, a 30-year-old female and a 60-year-old female with hypertension. First, the fresh blood samples were centrifuged for 10 min at 1,500 r·min^{-1}. Then the filtrates were centrifuged for 30 min at 3,000 r·min^{-1} in 30 kDa Amicon cells to obtain transparent serum. The obtained serum samples were diluted 4 times with Milli-Q water to make the GSH concentration of the detecting system in the linear range for detection. The specific detection method carried out according to Section 2.4. The concentrations of GSH were obtained by standard addition method.

3 Results and discussion

3.1 The crystal structures and morphologies of MnO_2 oxidase mimics

In order to identify the crystal phases of the samples, the MnO_2 oxidase mimics were tested by XRD. As shown in Fig. 1, diffraction peaks of the three MnO_2 samples matched well with the typical α-MnO_2 (JCPDS 44-0141), β-MnO_2 (JCPDS 24-0735) and γ-MnO_2 (JCPDS 14-0644) structures, respectively. There was not any other diffraction peak in the XRD patterns, suggesting that α, β, γ-MnO_2 crystal phases with high purity had been prepared successfully.

The physicochemical properties of MnO_2 with different crystal phases were shown in Table 1. γ-MnO_2 had both the maximum specific surface area (60.2 m^2·g^{-1}) and the minimum particle size (18.7 nm). For α-MnO_2 and β-MnO_2 samples, the specific surface areas were similar (30.6 vs. 33.7 m^2·g^{-1}), while β-MnO_2 had smaller particle size (30.4 vs. 24.7 nm). Figure 2 shows that all of the MnO_2 samples were assembled to form the same morphology, nanorods. α-MnO_2 nanorods were 15–95 nm in diameter and 0.27–1.3 μm in length. β-MnO_2 nanorods were 40–130 nm in diameter and 0.64–2.78 μm in length. γ-MnO_2 nanorods were 18–105 nm in diameter and 0.2–0.7 μm in length.

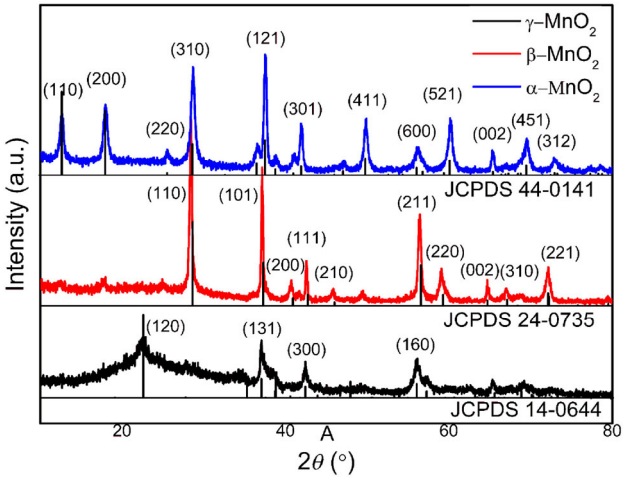

Figure 1 XRD patterns of MnO_2 different crystal phases.

3.2 Activities of MnO_2 oxidase mimics of different crystal phases

TMB was chosen as the substrate to test the activities of MnO_2 nanorods oxidase mimics. Figure 3(a) shows that α, β,

Table 1 Physical-chemical properties and activities of MnO_2 oxidase mimics with different crystal phases

Oxidase mimics	S_{BET} (m^2·g^{-1})	D^a (nm)	Mn^{4+}/Mn^{3+}	$O_{abs}/O_{-OH}/O_{latt}$	$V_{max}{}^b$ (μM·s^{-1})	$K_m{}^b$ (μM)	$K_{cat}{}^{b,c}$ (μmol·m^{-2}·s^{-1})
α-MnO_2	30.6	30.4	37/63	7/18/75	5.63/0.45	0.11/0.25	30.91/2.49
β-MnO_2	33.7	24.7	68/32	7/11/82	16.80/0.30	3.45/1.17	83.75/1.50
γ-MnO_2	60.2	18.7	30/70	9/14/77	1.58/0.36	0.93/1.14	4.41/1.00

[a] Calculated by Scherrer formula; [b] V_{max} or K_m of MnO_2 for TMB oxidation in air/N_2; [c] catalytic constant (per surface area of MnO_2) equals to the moles of TMB oxidized per unit time per unit specific surface area.

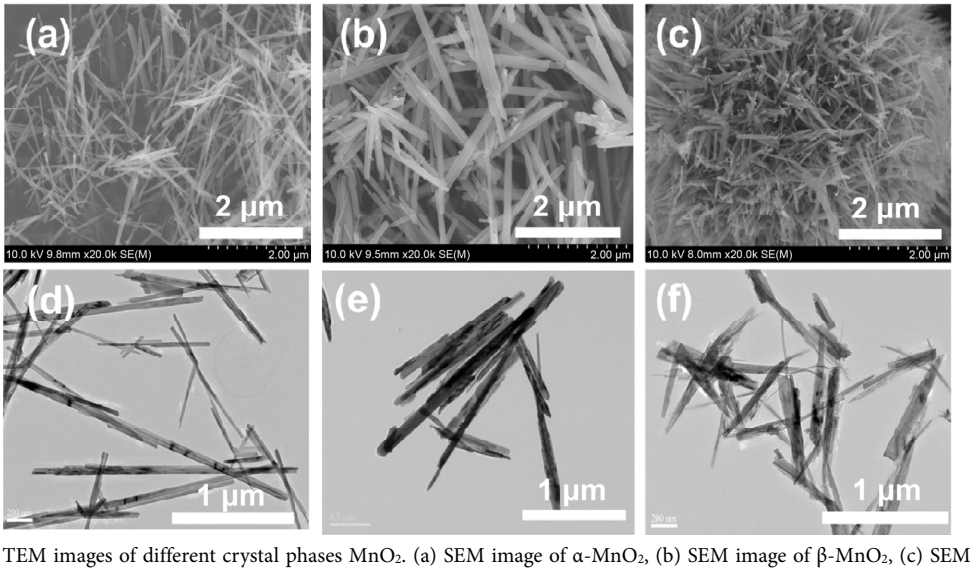

Figure 2 SEM and TEM images of different crystal phases MnO_2. (a) SEM image of α-MnO_2, (b) SEM image of β-MnO_2, (c) SEM image of γ-MnO_2, (d) TEM image of α-MnO_2, (e) TEM image of β-MnO_2, (f) TEM image of γ-MnO_2.

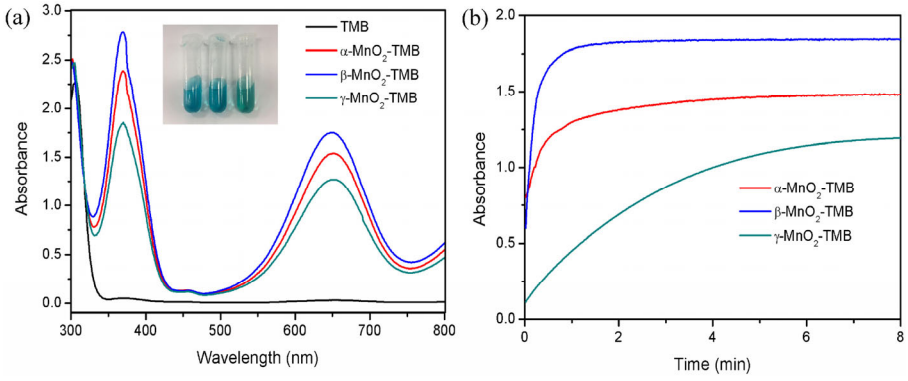

Figure 3 Activity test of MnO_2 oxidase mimics with different crystal phases, using TMB as the substrate. (a) UV–Vis absorbance of TMB oxidation catalyzed by α, β, γ-MnO_2. Insert: the TMB solutions catalyzed by α, β, γ-MnO_2 for 20 min, respectively. (b) The absorbance of TMB solution catalyzed by α, β, γ-MnO_2 as oxidase mimics at 652 nm within 8 min. The reaction conditions were: 1 mL of NaAc-HAc buffer with pH 4.0, 1 mL of 1.25 mM TMB solution, and 0.1 mL of 0.125 g·L^{-1} MnO_2 suspension.

γ-MnO_2 could all catalyze the oxidation of colorless TMB to blue oxTMB with an absorption peak at 652 nm, showing oxidase activity. Figure 3(b) shows that α-MnO_2 and β-MnO_2 catalyzed TMB instantaneously, reaching 90% of the maximum conversion in 0.5 and 1 min, respectively. The reaction rate of TMB catalyzed by γ-MnO_2 was relatively lower, reaching 90% of the maximum conversion after more than 5 min. According to the final maximum absorbance, the catalytic activities of the MnO_2 samples could be listed as β-MnO_2 > α-MnO_2 > γ-MnO_2.

However, the initial reaction rates (v_0), tested in the similar conditions except for the concentration of TMB solutions ([TMB]), were somehow different (Fig. 4(a)). The v_0 values were obtained by the average absorbance in the first 5 s (Fig. S1 in the Electronic Supplementary Material (ESM)) based on Lambert-Beer law. The v_0 of α-MnO_2 was the highest, followed by that of β-MnO_2 and γ-MnO_2 within the testing range ([TMB] < 1.7 mM). Although the values of v_0 of MnO_2 samples all increased with the increase of [TMB], v_0 of β-MnO_2 was the most sensitive to the change of [TMB]. The reason might be that diffusion was the control factor for the reaction process of β-MnO_2-TMB system under the testing conditions.

To verify this hypothesis, the zeta potentials and hydrodynamic size distributions of MnO_2 samples in buffer solution (NaAc-HAc buffer of pH 4.0:water = 1:1 v/v) were measured by DLS technique. As shown in Fig. S2 in the ESM, the zeta potentials of α, β, γ-MnO_2 were comparable and closed to zero (−3.98, −4.59 and −3.86 mV), indidating they were easy to form aggregates [29]. As shown in Fig. S3 in the ESM, the size distributions of the formed aggregates of α, β, γ-MnO_2 were about 150–350, 300–600 and 200–350 nm, repectively. β-MnO_2 aggregates had largest size, resulting in a worst diffusion coefficient in the reaction system [30] and thus a diffusion controlled reaction process of β-MnO_2-TMB system.

To further study the ability of MnO_2 oxidase mimics to bind and catalyze substrates, the Michaelis constant (K_m) and maximum reaction rate (V_{max}) were investigated using the Lineweaver-Burk plots (Fig. 4(b)) and listed in Table 1. The K_m values of α-, β- and γ-MnO_2 were 0.11, 3.45 and 0.93 μM, respectively. It indicated that α-MnO_2 had the best affinity for the substrate, TMB. Although β-MnO_2 had the worst substrate affinity, its V_{max} was the largest, 16.80 μM·s^{-1}, 3.0 and 10.6 times of those of α-MnO_2 (5.63 μM·s^{-1}) and γ-MnO_2 (1.58 μM·s^{-1}). The highest V_{max} of β-MnO_2 indicated that it had the strongest oxidation capacity, agreed with the fact that β-MnO_2 was the most active one for TMB oxidation with time prolonged.

To compare the intrinsic activities of α-, β- and γ-MnO_2, the catalytic constants (K_{cat}) of three MnO_2 oxidase mimics were calculated. Considering that only the surface of nanoparticles was involved in the reaction, the moles of TMB oxidized per unit time per unit specific surface area was calculated by Eq. (1) as K_{cat} when the oxidase mimics were saturated with TMB. The values of K_{cat} were 83.75, 30.91 and 4.41 μmol·m^{-2}·s^{-1} for β-MnO_2, α-MnO_2 and γ-MnO_2, respectively (Table 1). The K_{cat} of β-MnO_2 was 2.7 and 19.0 times of those of α-MnO_2 and γ-MnO_2. It indicated that the regulation of crystal phases was an effective way to modulate the characteristics of the active sites and thus the activity for desired enzyme mimics. Moreover, β-MnO_2 maintained a good reactivity in a wide range of pH, temperature, [TMB] and β-MnO_2 concentration, providing a prospective future for practical applications (Fig. S4 in the ESM).

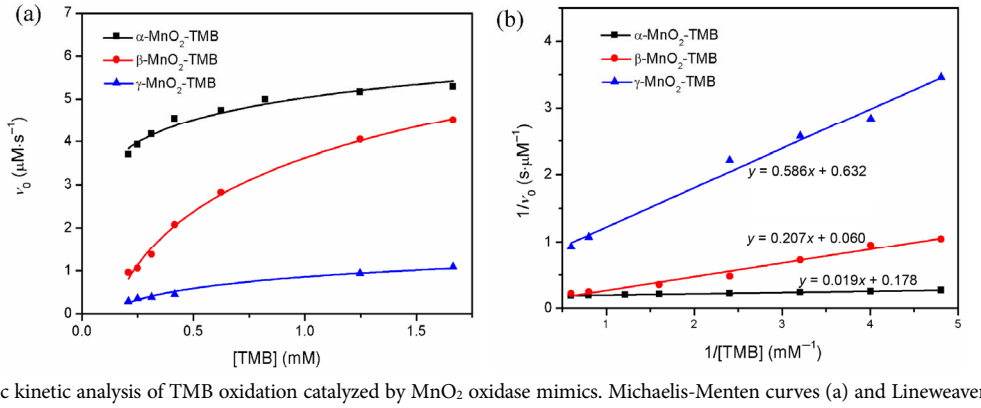

Figure 4 Enzymatic kinetic analysis of TMB oxidation catalyzed by MnO_2 oxidase mimics. Michaelis-Menten curves (a) and Lineweaver-Burk plots (b) for catalytic oxidation of TMB catalyzed by α, β, γ-MnO_2. The reaction conditions were: 1 mL of NaAc-HAc buffer with pH 4.0, 1 mL of TMB solution with different concentrations, 0.1 mL of 0.125 g·L^{-1} MnO_2 suspension, and the reaction temperature was 25 °C.

$$K_{cat} = V_{max}/(S_{BET}\cdot[MnO_2]) \quad (1)$$

where V_{max} is the maximum reaction rate of MnO_2; S_{BET} is the specific surface area of MnO_2, and $[MnO_2]$ is the concentration of MnO_2 in reaction system.

3.3 The surface chemical properties of MnO_2 samples and active species in the MnO_2-TMB system

It was well known that the surface chemical properties had an important influence on the performance of nano-enzyme catalysts. To clarify the mechanism of the structure–activity relationship of MnO_2 oxidase mimics, α, β, γ-MnO_2 with identical morphology but entirely different in activity, were characterized by H_2-TPR and XPS.

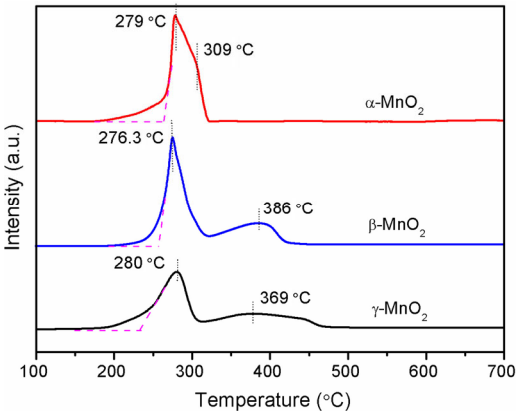

Figure 5 H_2-TPR profiles of α, β, γ-MnO_2.

The H_2-TPR results are given in Fig. 5. All of the three MnO_2 samples showed obvious reduction peaks centered at 275–280 °C, which could be attributed to the reduction of $MnO_2 \rightarrow Mn_3O_4$. For β- and γ-$MnO_2$, the second reduction peak showed at ca. 370 °C, which could be attributed to the reduction of $Mn_3O_4 \rightarrow MnO$ [28]. The second reduction peak of α-MnO_2 appeared at ca. 309 °C, shifting to the relatively low temperature and overlapping partly with the first reduction peak. It was worth noting that all of the three MnO_2 samples showed significantly widened and weakened reduction peaks below 270 °C. This indicated that there were large numbers of hydroxyl groups on the surface of the samples [31].

XPS spectra were used to further characterize the chemical states of Mn and O on the surface of MnO_2 oxidase mimics. The results in Fig. 6(a) and Table 1 showed that there were three kinds of O species on the surface of all the three MnO_2 samples, i.e. lattice oxygen (O_{latt}) of MnO_2 (binding energy of ~ 529.7 eV), oxygen of surface hydroxyl (O_{-OH}) (binding energy of ~ 531.0 eV) [32, 33] and oxygen of absorbed water (O_{abs}) (binding energy of ~ 532.0 eV) [34]. This result was consistent with the H_2-TPR characterization, indicating that there were a large number of surface hydroxyl groups. Surface hydroxyl contents (Table 1) were 18%, 11% and 14% for α-, β- and γ-MnO_2, respectively.

The XPS characterization results of Mn2p are shown in Fig. 6(b) and Table 1. For all the three MnO_2 samples, there were two kinds of Mn species, Mn^{3+} and Mn^{4+}, corresponding to the binding energy of $Mn2p_{3/2}$ at ~ 642.2 and ~ 643.6 eV, respectively [35–37]. However, there were significant differences in the ratio of Mn^{3+} and Mn^{4+} (Table 1). β-MnO_2 had the highest surface Mn^{4+} content of 68% (α-MnO_2 37% and γ-MnO_2 30%). The varying degrees of Mn^{3+} on the surface of MnO_2 symples were mainly due to the n-type semiconducting nature of MnO_2 to generate some MnOOH on their surfaces [38, 39].

ROS were often involved in TMB oxidation [40]. The ESR spectra (Fig. S5 in the ESM) showed that $\cdot O_2^-$, ·OH, and $^1O_2$ were all produced in α, β, γ-MnO_2 reaction systems. However, as shown in Fig. S6 in the ESM, it was noteworthy that the conversion of TMB oxidation remained above 65% for β-MnO_2-TMB system even in the case of adding three kinds of ROS scavengers together. According to previous reports, surface hydroxyls were beneficial to the oxidation reactions [41, 42]. They were more active than other oxygen species and could effectively promote oxidation reactions [43]. Therefore, the surface hydroxyls may be essential for TMB oxidation catalyzed by MnO_2.

The oxidation of TMB catalyzed by MnO_2 in a non-oxygen environment was performed further. As shown in Fig. 7 and Fig. S7 in the ESM, and Table 1, all of the three MnO_2 oxidase mimics could catalyze the TMB to oxTMB. It proved that the surface hydroxyls were directly involved in the oxidation reaction, since they were the only active oxygen species in inert atmosphere. The K_m values of α, β, γ-MnO_2 were 0.25, 1.17, 1.14 μM respectively, suggesting the affinity for TMB in sequence of α-MnO_2 > γ-MnO_2 > β-MnO_2, the same in air conditions. Furthermore, surface hydroxyls may improve the affinity between the MnO_2 and TMB, since the sequence of affinity for TMB both in inert and in air conditions was always consistent with that of surface hydroxyls of MnO_2 (Table 1).

The V_{max} of α-MnO_2, β-MnO_2 and γ-MnO_2 for TMB oxidation were 0.45, 0.30 and 0.36 $\mu M \cdot s^{-1}$, respectively (Table 1). Comparing to the reaction in air, the V_{max} values of all the three oxidase mimics decreased dramatically, about 92%, 98% and 77%, respectively (Table 1). For β-MnO_2, which had the highest V_{max} in air, V_{max} in inert atmosphere even became the lowest one in the three. And the K_{cat} of α-MnO_2, β-MnO_2 and γ-MnO_2 in inert condition for TMB oxidation were 2.49, 1.50 and 1.00 $\mu mol \cdot m^{-2} \cdot s^{-1}$, respectively (Table 1). The situation of K_{cat} values was similar to V_{max}. The more Mn^{4+} on the surface

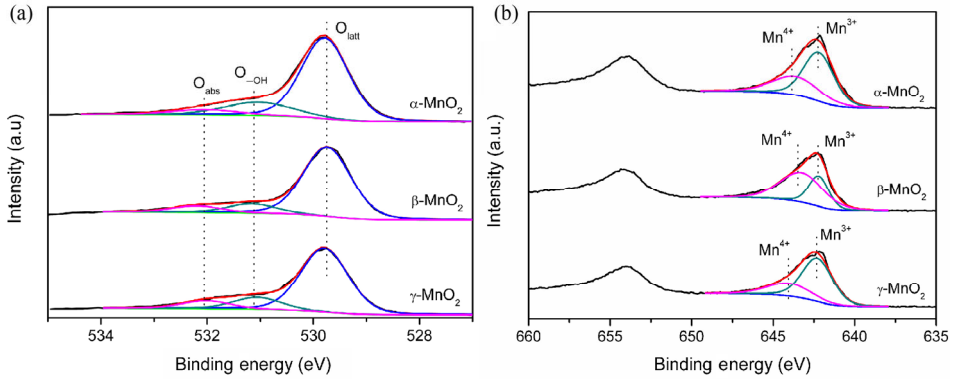

Figure 6 XPS spectra of α, β, γ-MnO_2. (a) O1s XPS spectra of α, β, γ-MnO_2. (b) Mn2p XPS spectra of α, β, γ-MnO_2.

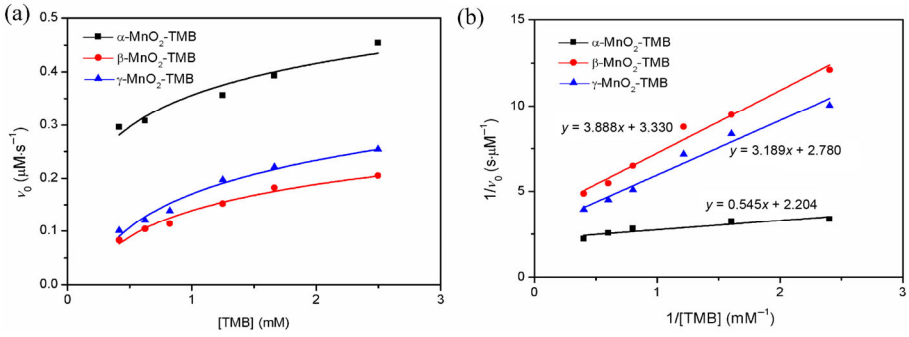

Figure 7 Enzymatic kinetic analysis of TMB oxidation catalyzed by MnO_2 oxidase mimics without dissolved oxygen. Michaelis-Menten curves (a) and Lineweaver-Burk plots (b) for catalytic oxidation of TMB by α, β, γ-MnO_2. The reaction conditions were: 1 mL of NaAc-HAc buffer with pH 4.0, 1 mL of TMB solution with different concentrations, 0.1 mL of 0.125 g·L^{-1} MnO_2 suspension, and the reaction temperature was 25 °C, and all solutions were purged by N_2 for at least one hour.

of MnO_2, the larger decrease in V_{max} and K_{cat} values happened (Table 1). Therefore, Mn^{4+} played an important role in the activities of MnO_2 oxidase mimics. According to the above discussion that the surface hydroxyls were the main species of TMB oxidation, it could be concluded that Mn^{4+} was beneficial to the regeneration of surface hydroxyl groups [37, 44], thereby improving oxidation reactivity. This might be the reason that β-MnO_2 had the weakest affinity with TMB yet a moderate v_0 and the highest V_{max} among three MnO_2 samples.

Besides, the K_{cat} values in inert condition did not strictly follow the order of surface hydroxyl. The possible reasons included: 1) Little amount of air leaked into the systems during the testing process, 2) water as a relative inert oxygen species could be activated by Mn^{4+} [45, 46]. Furthermore, taking β-MnO_2 as the representative, longing reaction time to reach a steady state in the inert atmosphere, the absorbance of the system at 652 nm was 0.7 (Fig. S8 in the ESM). Then open the cover of the colorimetric dish to unseal the system. The absorbance of the system at 652 nm increased gradually to 1.1 after 4 h in air (Fig. S8 in the ESM). It indicated TMB could be further oxidized in air, which demonstrated that the surface hydroxyls were regenerated by Mn^{4+} in the presence of dissolved oxygen in reaction system.

3.4 Discussion on the mechanism of catalytic oxidation

Due to the advantages of stability, economy and mass production possibility, enzyme mimics have a brilliant application prospect in the field of biomedicine. Catalytic reactions occur on the surface of the enzyme mimics, so the physical and chemical properties of the surface have a significant impact on the catalytic activity. In this study, the goal of controllable synthesis of MnO_2 with different crystal phase structures was achieved to regulate the surface physical and chemical properties. The structure–activity relationship of MnO_2 oxidase mimics was studied to provide theoretical insight and guidance for the rational design and development of efficient MnO_2 and other enzyme mimics.

In order to exclude the influence of morphology on activity, α-, β- and γ-MnO_2 nanorods with identical morphology but different crystal structures were prepared (Figs. 1 and 2). Table 1 showed that γ-MnO_2 had the largest specific surface area (60.2 $m^2 \cdot g^{-1}$) and the smallest particle size (18.7 nm). The specific surface areas of α- and β-MnO_2 were similar (30.6 vs. 33.7 $m^2 \cdot g^{-1}$), but the particle size of β-MnO_2 was slightly smaller than that of α-MnO_2 (30.4 vs. 24.7 nm). However, Fig. 3(b), as mentioned above, shows that the catalytic oxidation performance was in the order of β-MnO_2 > α-MnO_2 > γ-MnO_2, denying that the specific surface area or the particle size were the fundamental impacting factors of the activity of MnO_2 enzyme mimics.

Compared to ROS, surface hydroxyls were more important in oxidation of TMB catalyzed by MnO_2. Surface hydroxyls could oxidize TMB directly in a non-oxygen environment (Fig. 7 and Fig. S7 in the ESM, and Table 1). The K_m values of α, β, γ-MnO_2 in air (0.11, 3.45, 0.93 μM) and in inert condition (0.25, 1.17, 1.14 μM) suggested the affinity for TMB in sequence of α-MnO_2 > γ-MnO_2 > β-MnO_2, same with the sequence of surface hydroxyls of MnO_2. These results indicated that surface hydroxyls were the active oxygen species in MnO_2 catalyzed oxidation of TMB, and improved the affinity of MnO_2 to TMB.

Comparing to the reaction in air, the V_{max}/K_{cat} values of α, β, γ-MnO_2 in inert decreased dramatically, about 92%, 98% and 77%, respectively (Table 1). For β-MnO_2, which had the highest V_{max} (K_{cat}) of 16.80 μM·s^{-1} (83.75 μmol·m^{-2}·s^{-1}) in air, V_{max} (K_{cat}) in inert atmosphere even became the lowest one in the three. The more Mn^{4+} on the surface of MnO_2, the larger decrease in V_{max} and K_{cat} values happened. Therefore, Mn^{4+} must play a vital role in regenerating hydroxyls during the reaction process.

Since the surface hydroxyls were limited, the oxidation of TMB in N_2 reached a steady state (Fig. S8 in the ESM). Further oxidation would occur when air was introduced into reaction system again (Fig. S8 in the ESM). It demonstrated further that the surface hydroxyls were the active oxygen species in TMB oxidation and they could be regenerated by Mn^{4+} in the presence of dissolved oxygen in reaction system.

Based on the above discussion, here a summary could be made. The catalytic oxidation of TMB is shown in Eq. (2). Although in the overall process, the precise mechanism of the formation and the utilization of oxygen related species are too complicated to identify [45], the reaction above could be probably divided into several possible reactions or steps (scheme shown in Fig. 8(a)): 1) the oxidation of TMB by surface hydroxyl groups (Eq. (3)); 2) the reduction of Mn^{4+} by H_2O and the regeneration of surface hydroxyl groups (Eq. (4)); 3) the oxidation of Mn^{3+} to Mn^{4+} by oxygen to complete a redox cycle (Eq. (5)).

$$TMB + O_2 \xrightarrow{MnO_2} oxTMB + H_2O \quad (2)$$

$$TMB + -OH_{sur} \rightarrow oxTMB + H_2O \quad (3)$$

$$Mn^{4+} + H_2O \rightarrow Mn^{3+} + H^+ + -OH_{sur} \quad (4)$$

$$4H^+ + O_2 + 2Mn^{3+} \rightarrow 2Mn^{4+} + 2H_2O \quad (5)$$

Given that all the testing conditions (temperature, dissolved oxygen, etc.) could be considered identical, and that Mn^{4+} and $-OH_{sur}$ related directly to Mn^{3+} and H^+ respectively, the overall

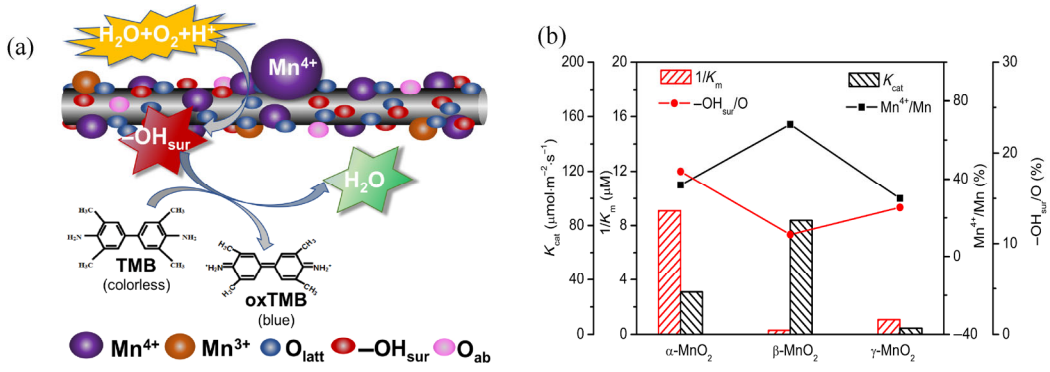

Figure 8 Analysis of effects of surface chemical properties on the oxidase performances of α, β, γ-MnO_2. (a) The mechanism scheme of TMB catalytic oxidation by MnO_2 as mimic. (b) Surface chemical properties on α, β, γ-MnO_2.

all reaction rate could be expressed as Eq. (6)

$$r = k\cdot[\mathrm{TMB}]^{a}\cdot(\alpha_{\mathrm{Mn^{4+}}})^{b}\cdot(\alpha_{-\mathrm{OH_{sur}}})^{c} \quad (6)$$

where r is reaction rate; k is reaction coefficient; a, b, c are impact index; [TMB] is concentration of TMB; $\alpha_{\mathrm{Mn^{4+}}}$ is atomic ratio of Mn^{4+} to Mn on the surface of MnO_2 nanorods; $\alpha_{-\mathrm{OH_{sur}}}$ is percentage of $-OH_{sur}$ in all surface oxygen species of MnO_2 nanorods.

The effects of surface chemical properties on the oxidase performances of MnO_2 oxidase mimics are shown in Fig. 8(b). The total catalytic activity depended on the complexed impacts of both $1/K_m$ (the expression of $-OH_{sur}$, affinity) and K_{cat} (the expression of both the amount of $-OH_{sur}$ as well as Mn^{4+}, ability to regenerate $-OH_{sur}$). At the beginning phase of the oxidation, α-MnO_2 with more $-OH_{sur}$ had a faster reaction rate, even though its Mn^{4+} content was much lower. With the reaction going on with a short period, $-OH_{sur}$ of α-MnO_2 decreased much faster than that of β-MnO_2, thus β-MnO_2 system surpassed in the reaction rate. The excellent catalytic activity of β-MnO_2 in TMB oxidation was due to the synergistic effect of surface hydroxyl and Mn^{4+}. γ-MnO_2 had neither good affinity nor abundant surface Mn^{4+} content, reasonably resulting in the lowest maximum reaction rate. Since the effect of other factors had been excluded, surface Mn^{4+} could be considered qualitatively the dominant influencing factor in this catalytic oxidation system. Moreover, it also proved that the regulation of crystal phases was an effective way to modulate the catalytic performance of MnO_2 enzyme mimics.

4 Detection of GSH

Cancer, AIDS and neurodegenerative diseases are related to abnormal GSH level [9–12]. Rapid, convenient and sensitive detection of GSH is of great significance in clinical diagnosis [10–13]. As GSH could simultaneously reduce oxTMB and MnO_2 to produce colorless TMB and inert Mn^{2+} respectively [13, 47], a colorimetric system of β-MnO_2-TMB-GSH was developed for GSH detection by using β-MnO_2, the oxidase mimic with the best activity. In the presence of GSH, the absorbance at 652 nm of β-MnO_2-TMB-GSH system was significantly reduced (Fig. 9(a)), indicating that the system was feasible to detect GSH. The linear analysis of the detection method was performed and the result was shown in Fig. 9(b). The ΔA value ($A - A_0$, A and A_0 were the absorbances of system at steady state before and after GSH addition) at the wavelength of 652 nm gradually increased with the increase of the concentration of GSH in the system. There was a good linear relationship between ΔA and GSH concentration when the GSH concentration is in the range of 0.11–0.45 μM. The linear regression equation is $\Delta A = 0.0305\ [\mathrm{GSH}] + 0.0416$ ($r^2 = 0.997$, $n = 14$), and the detection limit (LOD) is 0.1 μM. Compared with the existed GSH colorimetric detection method (Table 2), the detection method based on β-MnO_2 has a wider linear range and a lower detection limit, and the similarity sensitivity as the fluorescence method [53–55].

In order to investigate the selectivity of β-MnO_2-TMB system for GSH, the effects of potential interferences of bio-ions, glucose, AA, Cys and other amino acids in human serum to the system were further studied. As shown in Fig. S9 in the ESM, although they were at 100 times the concentration of GSH, interferences of less than 5% were observed after addition them to the GSH detection system, except for AA and Cys. Although AA and Cys have a certain degree of inhibition on the activity of β-MnO_2 oxidase [23, 40], considering their biological concentration is far lower than GSH, it is unlikely to have a significant impact on the detection of GSH.

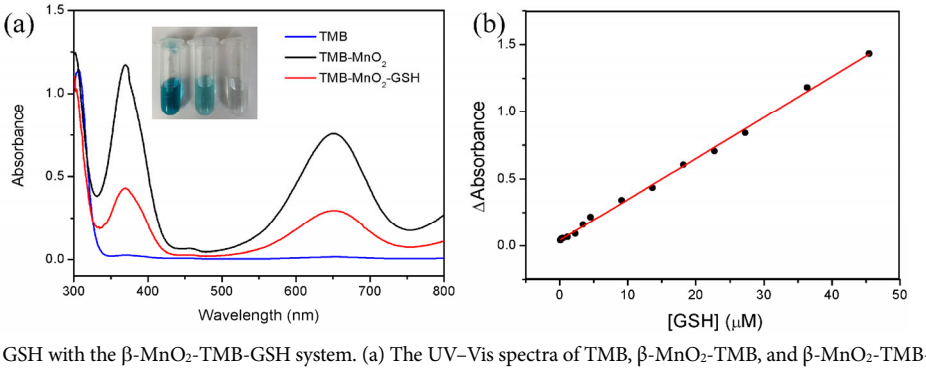

Figure 9 Detection of GSH with the β-MnO_2-TMB-GSH system. (a) The UV–Vis spectra of TMB, β-MnO_2-TMB, and β-MnO_2-TMB-GSH systems. (b) The calibration curve for GSH detection by β-MnO_2-TMB-GSH system. Test conditions: 1 mL of NaAc-HAc buffer with pH 4.0, 1 mL of 1.25 mM TMB solution, 0.1 mL of 0.125 g·L^{-1} β-MnO_2 suspension and 0.1 mL of GSH solution with different concentrations thoroughly reacted at 25 °C for 20 min.

Table 2 The detection ranges and limits of nano-enzymes for GSH detection

Nano-enzymes	Measurement method	Detection ranges (μM)	Detection limits (μM)	References
MnO_2-nanosheet	Colorimetry	1–25	0.3	[22]
MnO_2-nanowire	Colorimetry	0.3–15	0.11	[23]
Co, N-HPC	Colorimetry	0.05–30	0.036	[40]
Fe_3O_4	Colorimetry	3–30	3	[48]
Au	Colorimetry	2–25	0.42	[49]
Ag NPs-N-GQDs	Colorimetry	0.1–157.6	0.03	[50]
PtNPs@MnO_2	Colorimetry	0.2–11	0.05	[51]
SPB-MnO_2	Colorimetry	—	0.45	[14]
MnO_2-nanosheet	Colorimetry	10–100	0.5	[52]
$Eu(DPA)_3$@Lap-Tris	Fluorimetry	0.5–30	162	[53]
Au-Ag	Fluorimetry	1–10^4	0.2	[54]
GQDs–MnO_2	Fluorimetry	0.5–10	0.15	[55]
MnO_2-nanosheet	Electrochemical method	0.01–2	3.7 (nM)	[56]
NiPdNPs/GCE	Electrochemical method	0.5–3,000	0.5	[57]
Pt	Electrochemical method	19.9–300.7	22.8	[58]
Cu-CoHCF/GO/GCE	Electrochemical method	0.2–5	0.25	[59]
β-MnO_2	Colorimetry	0.11–45	0.1	This work

To evaluate practical application of the proposed method for detecting GSH level in biological environments, GSH content in three fresh human serum samples were detected. The test results in Table 3 showed that the recovery range was 98.17%–105.57%, with RSD < 5% (n = 6). The results indicated that the method proposed in this paper had high accuracy and reliability, and it was very feasible for detection of GSH in biological system.

5 Conclusions

In this paper, MnO_2 nanorods (α-, β- and γ-MnO_2) with the same morphology yet different crystal phases were prepared by hydrothermal method and the catalytic activities of them for TMB oxidation were investigated. Although the α-MnO_2 oxidase mimic had the best affinity with TMB and the highest initial reaction rate due to the highest content of surface hydroxyl, the β-MnO_2 oxidase mimic presented the largest K_{cat} (V_{max}) of 83.75 μmol·m^{-2}·s^{-1} (16.80 μM·s^{-1}), which was 1.7 (2.0) and 18.0 (9.6) times higher than those of α-MnO_2 and γ-MnO_2. The reason was that there were appropriate amount of hydroxyl groups and relative high content of Mn^{4+} on the surface of β-MnO_2. The surface hydroxyl group was conducive to the oxidation of TMB, while Mn^{4+} was beneficial to the regeneration of the surface hydroxyl groups. The synergistic effect of both factors significantly enhanced the reaction rate of β-MnO_2 oxidase mimic system. A β-MnO_2-TMB-GSH system was established to detect the content of GSH in the solution rapidly and sensitively by colorimetry. The system had a wide detection range of 0.11–45 μM and a low detection limit of 0.1 μM, and had been successfully applied to the detection of GSH in human serum samples. In this study, β-MnO_2 oxidase mimic with good performance was developed by adjusting crystal structure and surface physicochemical properties. The success of this strategy would also provide a possible way to develop other highly efficient nano-enzymes with other active species and/or in other application fields.

Acknowledgements

This work was supported by the National Key R&D Program of China (No. 2016YFA0202900), China Postdoctoral Science Foundation (No. 2018M642021), the National Natural Science Foundation of China (No. 21677095) and Minhang District Science and Technology Project of Shanghai (No. 2019MH-MS02).

Electronic Supplementary Material: Supplementary material (details of the test of initial reaction rate, Figs. S1 and S7; zeta potentials and hydrodynamic sizes of MnO_2, Figs. S2 and S3; details of the environment tolerance of β-MnO_2 oxidase mimic, Fig. S4; analysis of main active oxygen species in the process of reaction, Figs. S5 and S6; details of the sequential oxidation of TMB in N_2 and O_2, Fig. S8; the selective analysis of GSH by β-MnO_2-TMB system, Fig. S9) is available in the online version of this article at https://doi.org/10.1007/s12274-020-2680-5.

Table 3 The detection results of GSH in human serum samples

Samples	Original[a] (μM)	Added (μM)	Total[a] (μM)	Recovery	RSD
Serum 1	0.152 ± 0.009	0.2	0.364 ± 0.013	105.57%	3.17%
		0.4	0.558 ± 0.015	101.32%	2.71%
Serum 2	0.200 ± 0.007	0.2	0.411 ± 0.016	105.57%	3.83%
		0.4	0.595 ± 0.018	98.58%	2.23%
Serum 3	0.328 ± 0.016	0.2	0.524 ± 0.021	98.17%	4.07%
		0.4	0.732 ± 0.023	101.05%	3.13%

[a] Average ± standard deviation (n = 6).

References

[1] Hu, X.; Liu X. D.; Zhang, X. D.; Cao, H. Y.; Huang, Y. M. MnO_2 nanowires tuning of photoluminescence of alloy Cu/Ag NCs and thiamine enables a ratiometric fluorescent sensing of glutathione. *Sens. Actuators B: Chem.* **2019**, *286*, 476–482.

[2] Zhu, X. L.; Mao, X. X.; Wang, Z. H.; Feng, C.; Chen, G. F.; Li, G. X. Fabrication of nanozyme@DNA hydrogel and its application in biomedical analysis. *Nano Res.* **2017**, *10*, 959–970.

[3] Shoja, Y.; Rafati, A. A.; Ghodsi, J. Polythiophene supported MnO_2 nanoparticles as nano-stabilizer for simultaneously electrostatically immobilization of D-amino acid oxidase and hemoglobin as efficient bio-nanocomposite in fabrication of dopamine bi-enzyme biosensor. *Mater. Sci. Eng.: C.* **2017**, *76*, 637–645.

[4] Lai, W. Q.; Zeng, Q.; Tang, J.; Zhang, M. S.; Tang, D. P. A conventional chemical reaction for use in an unconventional assay: A colorimetric immunoassay for aflatoxin B_1 by using enzyme-responsive just-in-time generation of a MnO_2 based nanocatalyst. *Microchimica Acta* **2018**, *185*, 92.

[5] Amjadi, M.; Hallaj, T.; Kouhi, Z. An enzyme-free fluorescent probe based on carbon dots–MnO_2 nanosheets for determination of uric acid. *J. Photochem. Photobiol. A: Chem.* **2018**, *356*, 603–609.

[6] McVey, C.; Logan, N.; Thanh, N. T. K.; Elliott, C.; Cao, C. O. Unusual switchable peroxidase-mimicking nanozyme for the determination of proteolytic biomarker. *Nano Res.* **2019**, *12*, 509–516.

[7] Lu, S. C. Regulation of glutathione synthesis. *Mol. Aspects Med.* **2009**, *30*, 42–59.

[8] Franco, R.; Cidlowski, J. A. Apoptosis and glutathione: Beyond an antioxidant. *Cell Death Differ.* **2009**, *16*, 1303–1314.

[9] Michelet, F.; Gueguen, R.; Leroy, P.; Wellman. M.; Nicolas, A.; Siest, G. Blood and plasma glutathione measured in healthy subjects by HPLC: Relation to sex, aging, biological variables, and life habits. *Clin. Chem.* **1995**, *41*, 1509–1517.

[10] Zhang, D.; Yang, Z. H.; Li, H. J.; Pei, Z. C.; Sun, S. G.; Xu, Y. Q. A simple excited-state intramolecular proton transfer probe based on a new strategy of thiol-azide reaction for the selective sensing of cysteine and glutathione. *Chem. Commun.* **2016**, *52*, 749–752.

[11] Townsend, D. W.; Tew, K. D.; Tapiero, H. The importance of glutathione in human disease. *Biomed. Pharmacother.* **2003**, *57*, 145–155.

[12] Estrela, J. M.; Ortega, A.; Obrador, E. Glutathione in cancer biology and therapy. *Crit. Rev. Clin. Lab. Sci.* **2006**, *43*, 143–181.

[13] Deng, R. R.; Xie, X. J.; Vendrell, M.; Chang, Y. T.; Liu, X. G. Intracellular glutathione detection using MnO_2-nanosheet-modified upconversion nanoparticles. *J. Am. Chem. Soc.* **2011**, *133*, 20168–20171.

[14] Yang, Q. S.; Li, L.; Zhao, F.; Wang, Y. W.; Ye, Z. S.; Guo, X. H. Generation of MnO_2 nanozyme in spherical polyelectrolyte brush for colorimetric detection of glutathione. *Mater. Lett.* **2019**, *248*, 89–92.

[15] Shamsipur, M.; Safavi, A.; Mohammadpour, Z. Indirect colorimetric detection of glutathione based on its radical restoration ability using carbon nanodots as nanozymes. *Sens. Actuators B: Chem.* **2014**, *199*, 463–469.

[16] Fu, Y.; Zhang H. X.; Dai, S. D.; Zhi, X.; Zhang, J. L.; Li, W. Glutathione-stabilized palladium nanozyme for colorimetric assay of silver(I) ions. *Analyst* **2015**, *140*, 6676–6683.

[17] Han, K. N.; Choi, J. S.; Kwon, J. Gold nanozyme-based paper chip for colorimetric detection of mercury ions. *Sci. Rep.*. **2017**, *7*, 2806.

[18] Jiang, T.; Song, Y.; Du, D.; Liu, X. T.; Lin, Y. H. Detection of p53 protein based on mesoporous Pt–Pd nanoparticles with enhanced peroxidase-like catalysis. *ACS Sens.* **2016**, *1*, 717–724.

[19] Xie, J. X.; Zhang, X. D.; Wang, H.; Zheng, H. Z.; Huang, Y. M.; Xie, J. X. Analytical and environmental applications of nanoparticles as enzyme mimetics. *TrAC, Trends Anal. Chem.* **2012**, *39*, 114–129.

[20] Wei, H.; Wang, E. K. Nanomaterials with enzyme-like characteristics (nanozymes): Next-generation artificial enzymes. *Chem. Soc. Rev.* **2013**, *42*, 6060–6093.

[21] Liu, X.; Wang, Q.; Zhao, H. H.; Zhang, L. C.; Sun, Y. Y.; Lv, Y. BSA-templated MnO_2 nanoparticles as both peroxidase and oxidase mimics. *Analyst* **2012**, *137*, 4552–4558.

[22] Liu, J.; Meng, L. J.; Fei, Z. F.; Dyson, P. J.; Jing, X. N.; Liu, X. MnO_2 nanosheets as an artificial enzyme to mimic oxidase for rapid and sensitive detection of glutathione. *Biosens. Bioelectron.* **2017**, *90*, 69–74.

[23] Zhang, X. D.; Mao, X. X.; Li, S. Q.; Dong, W. F.; Huang, Y. M. Tuning the oxidase mimics activity of manganese oxides via control of their growth conditions for highly sensitive detection of glutathione. *Sens. Actuators B: Chem.* **2018**, *258*, 80–87.

[24] Xie, J. X.; Zhang, X. D.; Jiang, H.; Wang, S.; Liu, H.; Huang, Y. M. V_2O_5 nanowires as a robust and efficient peroxidase mimic at high temperature in aqueous media. *RSC Adv.* **2014,** *4*, 26046–26049.

[25] Liu, S. H.; Lu, F.; Xing, R. M.; Zhu, J. J. Structural effects of Fe_3O_4 nanocrystals on peroxidase-like activity. *Chem.—Eur. J.* **2011**, *17*, 620–625.

[26] Wan, Y.; Qi, P.; Zhang, D.; Wu, J. J.; Wang, Y. Manganese oxide nanowire-mediated enzyme-linked immunosorbent assay. *Biosens. Bioelectron.* **2012**, *33*, 69–74.

[27] Wang, R. H.; Li, J. H. Effects of precursor and sulfation on OMS-2 catalyst for oxidation of ethanol and acetaldehyde at low temperatures. *Environ. Sci. Technol.* **2010**, *44*, 4282–4287.

[28] Liang, S. H.; Teng, F.; Bulgan, G.; Zong, R. L.; Zhu, Y. F. Effect of phase structure of MnO_2 nanorod catalyst on the activity for CO oxidation. *J. Phys. Chem. C* **2008**, *112*, 5307–5315.

[29] Schwegmann, H.; Feitz, A. J.; Frimmel, F, H. Influence of the zeta potential on the sorption and toxicity of iron oxide nanoparticles on *S. cerevisiae* and *E. coli*. *J. Colloid Interface Sci.* **2010**, *347*, 43–48.

[30] Kätzel, U.; Vorbau, M.; Stintz, M.; Gottschalk-Gaudig, T.; Barthel, H. Dynamic light scattering for the characterization of polydisperse fractal systems: II. Relation between structure and DLS results. *Part. Part. Syst. Charact.* **2008**, *25*, 19–30.

[31] Otsuka, K.; Wang, Y.; Sunada, E.; Yamanaka, I. Direct partial oxidation of methane to synthesis gas by cerium oxide. *J. Catal.* **1998**, *175*, 152–160.

[32] Venkataswamy, P.; Jampaiah, D.; Mukherjee, D.; Aniz, C. U.; Reddy, B. M. Mn-doped ceria solid solutions for CO oxidation at lower temperatures. *Catal. Lett.* **2016**, *146*, 2105–2118.

[33] Yao, X. J.; Yu, Q.; Ji, Z. Y.; Lv, Y. Y.; Cao, Y.; Tang, C. J.; Gao, F.; Dong, L.; Chen, Y. A comparative study of different doped metal cations on the reduction, adsorption and activity of $CuO/Ce_{0.67}M_{0.33}O_2$ (M = Zr^{4+}, Sn^{4+}, Ti^{4+}) catalysts for NO + CO reaction. *Appl. Catal. B: Environ.* **2013**, *130–131*, 293–304.

[34] Reddy, B. M.; Bharali, P.; Saikia, P.; Park, S. E.; Van Den Berg, M. W. E.; Muhler, M.; Grünert, W. Structural characterization and catalytic activity of nanosized $Ce_xM_{1-x}O_2$ (M = Zr and Hf) mixed oxides. *J. Phys. Chem. C* **2008**, *112*, 11729–11737.

[35] Zhang, D. S.; Zhang, L.; Shi, L. Y.; Fang, C.; Li, H. R.; Gao, R. H.; Huang, L.; Zhang, J. P. *In situ* supported MnO_x–CeO_x on carbon nanotubes for the low-temperature selective catalytic reduction of NO with NH_3. *Nanoscale* **2013**, *5*, 1127–1136.

[36] Jian, Y. F.; Ma, M. D.; Chen, C. W.; Liu, C.; Yu, Y. K.; Hao, Z. P.; He, C. Tuning the micromorphology and exposed facets of MnO_x promotes methyl ethyl ketone low-temperature abatement: Boosting oxygen activation and electron transmission. *Catal. Sci. Technol.* **2018**, *8*, 3863–3875.

[37] Tang, W. X.; Wu, X. F.; Li, D. Y.; Wang, Z.; Liu, G.; Liu, H. D.; Chen, Y. F. Oxalate route for promoting activity of manganese oxide catalysts in total VOCs' oxidation: Effect of calcination temperature and preparation method. *J. Mater. Chem. A* **2014**, *2*, 2544–2554.

[38] Bhide, V. G.; Dani, R. H. Electrical conductivity in oxides of manganese and related compounds. *Physica* **1961**, *27*, 821–826.

[39] Kahil, H. Introduction to the dynamic theory of the (H^+, e^-) couple insertion in γ-MnO_2. *J. Solid State Electrochem.* **2000**, *4*, 107–120.

[40] Li, S. Q.; Wang, L. T.; Zhang, X. D.; Chai, H. X.; Huang, Y. M. A Co,N co-doped hierarchically porous carbon hybrid as a highly efficient oxidase mimetic for glutathione detection. *Sens. Actuators B: Chem.* **2018**, *264*, 312–319.

[41] Zhang, J.; Zhang, J. H.; Zhang, C. B.; He, H. Complete catalytic oxidation of ethanol over MnO_2 with different crystal phase structures. *Acta Phys. Chim. Sin.* **2015**, *31*, 353–359.

[42] Zhang, X. L.; Ye, J. H.; Yuan, J.; Cai, T.; Xiao, B.; Liu, Z.; Zhao, K. F.; Yang, L.; He, D. N. Excellent low-temperature catalytic performance of nanosheet Co-Mn oxides for total benzene oxidation. *Appl. Catal. A: Gen.* **2018**, *566*, 104–112.

[43] Cai, S. X.; Zhang, D. S.; Zhang, L.; Li, H. R.; Gao, R. H.; Shi, L. Y.; Zhang, J. P. Comparative study of 3D ordered macroporous $Ce_{0.75}Zr_{0.2}M_{0.05}O_{2-\delta}$ (M = Fe, Cu, Mn, Co) for selective catalytic reduction of NO with NH_3. *Catal. Sci. Technol.* **2014**, *4*, 93–101.

[44] Yang, J.; Liu, X. L.; Cao, H. B.; Shi, Y. C.; Xie, Y. B.; Xiao, J. D. Dendritic $BiVO_4$ decorated with MnO_x co-catalyst as an efficient hierarchical catalyst for photocatalytic ozonation. *Front. Chem. Sci. Eng.* **2019**, *13*, 185–191.

[45] Barber, J. Photosynthetic water splitting by the $Mn_4Ca^{2+}O_x$ catalyst of photosystem II: Its structure, robustness and mechanism. *Quart. Rev. Biophys.* **2017**, *50*, e13.

[46] Siegbahn, P. E. M. Quantum chemical studies of manganese centers in biology. *Curr. Opin. Chem. Biol.* **2002**, *6*, 227–235.

[47] Liu, X.; Wang, Q.; Zhang, Y.; Zhang, L. C.; Su, Y. Y.; Lv, Y. Colorimetric detection of glutathione in human blood serum based on the reduction of oxidized TMB. *New J. Chem.* **2013**, 37, 2174–2178.

[48] Ma, Y. H.; Zhang, Z. Y.; Ren, C. L.; Liu, G. Y.; Chen, X. G. A novel colorimetric determination of reduced glutathione in A549 cells based on Fe_3O_4 magnetic nanoparticles as peroxidase mimetics. *Analyst* **2012**, *137*, 485–489.

[49] Feng, J. Y.; Huang, P. C.; Shi, S. Z.; Deng, K. Y.; Wu, F. Y. Colorimetric detection of glutathione in cells based on peroxidase-like activity of gold nanoclusters: A promising powerful tool for identifying cancer cells. *Anal. Chim. Acta* **2017**, *967*, 64–69.

[50] Ju, J.; Zhang, R. Z.; Chen, W. Photochemical deposition of surface-clean silver nanoparticles on nitrogen-doped graphene quantum dots for sensitive colorimetric detection of glutathione. *Sens. Actuators B: Chem.* **2016**, *228*, 66–73.

[51] Liu, J.; Meng, L. J.; Fei, Z. F.; Dyson, P. J.; Zhang, L. On the origin of the synergy between the Pt nanoparticles and MnO_2 nanosheets in Wonton-like 3D nanozyme oxidase mimics. *Biosens. Bioelectron.* **2018**, *121*, 159–165.

[52] Di, W. H; Zhang, X.; Qin, W. P. Single-layer MnO_2 nanosheets for sensitive and selective detection of glutathione by a colorimetric method. *Appl. Surf. Sci.* **2017**, *400*, 200–205.

[53] Chen, X.; Wang, Y. R.; Chai, R.; Xu, Y.; Li, H. R.; Liu, B. Y. Luminescent lanthanide-based organic/inorganic hybrid materials for discrimination of glutathione in solution and within hydrogels. *ACS Appl. Mater. Interfaces* **2017**, *9*, 13554–13563.

[54] Zhai, Q. F.; Xing, H. H.; Fan, D. Q.; Zhang, X. W.; Li, J.; Wang, E. K. Gold-silver bimetallic nanoclusters with enhanced fluorescence for highly selective and sensitive detection of glutathione. *Sens. Actuators B: Chem.* **2018**, *273*, 1827–1832.

[55] Yan, X.; Song, Y.; Zhu, C. Z.; Song, J. H.; Du, D.; Su, X. G.; Lin, Y. H. Graphene quantum dot-MnO_2 nanosheet based optical sensing platform: A sensitive fluorescence "turn off-on" nanosensor for glutathione detection and intracellular imaging. *ACS Appl. Mater. Interfaces* **2016**, *8*, 21990–21996.

[56] Gao, W. Y.; Liu, Z. Y.; Qi, L. M.; Lai, J. P.; Kitte, S. A.; Xu, G. B. Ultrasensitive glutathione detection based on lucigenin cathodic electrochemiluminescence in the presence of MnO_2 nanosheets. *Anal. Chem.* **2016**, *88*, 7654–7659.

[57] Zhang, H. Z.; Zhang, L.; Ding, Y.; Zhang, W. Q.; Zhang, X.; Shen, Y. H.; Yang, F. C. Determination of glutathione based on NiPd nanoparticles mediated with acetaminophen. *Anal. Methods* **2016**, *8*, 3000–3005.

[58] Valero-Ruiz, E.; González-Sánchez, M. I.; Batchelor-McAuley, C.; Compton, R. G. Halogen mediated voltammetric oxidation of biological thiols and disulfides. *Analyst* **2016**, *141*, 144–149.

[59] Hassanvand, Z.; Jalali, F. Electrocatalytic determination of glutathione using transition metal hexacyanoferrates (MHCFs) of copper and cobalt electrode posited on graphene oxide nanosheets. *Anal. Bioanal. Chem. Res.* **2018**, *5*, 115–129.